

Tunable Flux-Matching Effects in High- T_c Superconductors with Nonuniform Pinning Arrays

J. Trastoy,¹ C. Ulysse,² R. Bernard,¹ M. Malnou,³ N. Bergeal,³ J. Lesueur,³ J. Briatico,¹ and Javier E. Villegas^{1,*}

¹*Unité Mixte de Physique, CNRS, Thales, Univ. Paris-Sud, Université Paris-Saclay, 91767 Palaiseau, France*

²*CNRS, Laboratoire de Photonique et de Nanostructures, route de Nozay, 91460 Marcoussis, France*

³*LPEM, ESPCI-CNRS-UPMC, PSL Research University, 10 rue Vauquelin, 75231 Paris, France*

(Received 29 May 2015; revised manuscript received 8 September 2015; published 12 November 2015)

We experimentally study superconducting $\text{YBa}_2\text{Cu}_3\text{O}_7$ thin films with artificial vortex pinning arrays created via masked ion irradiation. In particular, we compare a series of arrays (2D periodic non-Bravais lattices) in which the density of pinning sites is nonuniform within the unit cell. The series consists of variants of a canonical array, which is gradually deformed by varying the separation between pinning centers within the unit cell. Interestingly, the array deformation produces a very striking evolution of magnetoresistance flux-matching effects, which strongly depend on temperature. The key to this unusual behavior is the nanoscale spatial modulation of the superconducting critical temperature produced via masked ion irradiation. The hereby-demonstrated tunability of the flux-matching effects brings possibilities to the field of vortex manipulation in high-temperature superconductors.

DOI: 10.1103/PhysRevApplied.4.054003

I. INTRODUCTION

Nanopatterning of superconductors is a thoroughly investigated approach to create vortex pinning arrays and to finely tailor the energy landscape for magnetic flux quanta. On the one hand, this provides a versatile model to study the physics of a manifold of interacting elastic elements on an arbitrary energy landscape. In the case of high-temperature superconductors, that playground is further enriched by the presence of sizable thermal activation [1]. Nanopatterned superconductors indeed allow a variety of fundamental studies on generic physical problems, e.g., commensurability [2–8], rectification [9,10], jamming [11,12], or avalanches [13,14], which concern not only vortices but a variety of systems [15–21]. In addition, the increased ability to manipulate vortices via artificial pinning paves the way towards technological applications, such as superconducting diodes [9,10], signal processors [22], logic devices [23,24], etc. These applications rely on the ability to design the geometry of the artificial pinning potential. In this context, the possibility to reversibly reconfigure the pinning landscape via external parameters is especially interesting [25]. Here we realize a system in which the effective pinning array geometry can be tuned by using the temperature as a knob.

Most of the large body of research on the area of artificial ordered pinning focuses on regular, periodic arrays of vortex pinning centers [3,5–7]. In the presence of these arrays, a sudden drop of the mixed-state magnetoresistance is observed at a magnetic field—the matching field—for

which the vortex density equals the density of the pinning sites. However, field-matching effects and enhanced vortex pinning are observed also with quasiperiodic [26,27] and partially disordered pinning arrays [28–30]. In the present paper, we study an intermediate situation. We initially consider a periodic non-Bravais pinning array, which has fourfold symmetry and in which the pinning-site distribution is nonuniform within the array unit cell [Fig. 1(a)]. Then we study variations of the same array in which the fourfold symmetry is suppressed [Figs. 1(b)–1(d)] by varying the distance between some of the pinning sites inside the array unit cell. As we show below by comparing a series of arrays, the step-by-step deformation of the initial array yields a striking evolution in the measured matching fields. This is because the closest pinning sites tend to behave as a single (composite) site as their separation is gradually shortened. Interestingly, this tendency can be broken upon lowering the temperature, which yields to a temperature tunability of the pinning array geometry. This unique possibility opens horizons within the field of fluxtronics [9,10,22–24], in which controlled vortex motion using artificial energy landscapes is used to create functionalities. For instance, vortex diodes [10] and superconducting signal rectifiers [22] are realized by using asymmetric pinning arrays. The approach developed here provides a means to control the asymmetry (and thus the signal rectification), using the temperature as a handle.

II. EXPERIMENT

The 50-nm-thick $\text{YBa}_2\text{Cu}_3\text{O}_{7-\delta}$ (YBCO) films are grown by pulsed laser deposition on top of SrTiO_3 (001) substrates. The 40- μm -wide bridges are photolithographed and

*javier.villegas@thalesgroup.com

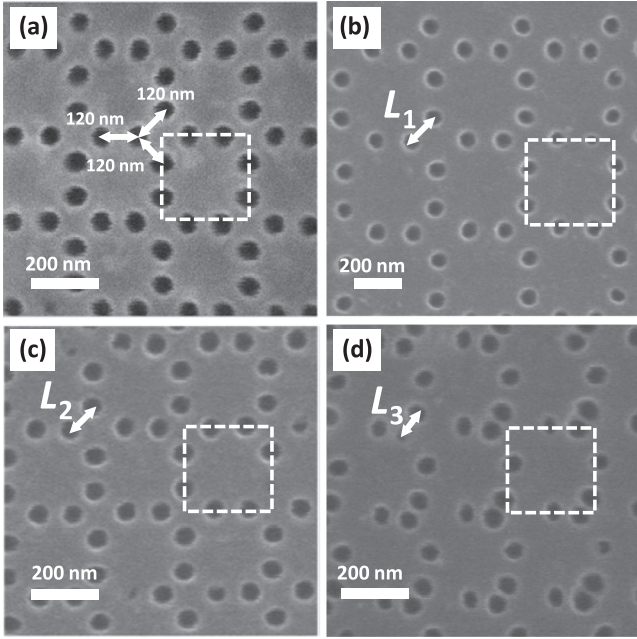


FIG. 1. Scanning electron microscopy images of the masks employed for O^+ irradiation with different hole arrays. (a) Canonical array with fourfold symmetry and for which every hole's first neighbors are at the same distance, as indicated by the white arrows. (b)–(d) Variations of the canonical array, in which the distance marked as L_i , $i = \{1, 2, 3\}$, is gradually reduced relative to the other distances. The array unit cell is indicated with a white dashed square in each case.

dry etched for electrical transport measurements, with voltage probes $200 \mu\text{m}$ apart. Gold contact pads are created by sputtering deposition. Subsequently, non-Bravais periodic pinning arrays are patterned in the YBCO by using a masked ion irradiation technique. Details can be found elsewhere [31]. In summary, the YBCO surface is covered with a thick layer of PMMA resist. By using electron-beam lithography, an array of nanometric holes is defined on the resist. The nanoporated PMMA is then used as a mask through which the sample is irradiated by using 110-keV oxygen ions (fluence of 5×10^{13} ions/cm²). This creates point defects in the YBCO areas exposed by the mask's holes. These defects depress superconductivity locally, so that the irradiated YBCO areas under the holes in the mask behave as strong pinning sites [31].

Figure 1 shows scanning electron microscopy images of the masks used for the present experiments. The hole diameter is approximately 70 nm. The canonical array is shown in Fig. 1(a), while the three others [Figs. 1(b)–1(d)] are variants of it. All of them are periodic non-Bravais arrays, in which the unit cell—depicted by a white dashed square—contains four pinning sites (less than 5% of the array unit cells present missing pinning sites due to errors during electron-beam lithography). The number of vortices per array unit cell is given by $n = B/B_\phi$, where $B_\phi = \phi_0/S$ ranges between 0.0104 and 0.0234 T for the studied

TABLE I Characteristic parameters B_ϕ , transition-onset temperature $T_{C,\text{onset}}$, zero-resistance temperature T_{C0} and normal state resistivity ρ_N for samples A–D, corresponding to the arrays shown in Figs. 1(a)–1(d), respectively.

Sample	B_ϕ (T)	$T_{C,\text{onset}}$ (K)	T_{C0} (K)	ρ_N ($10^{-6} \Omega\text{m}$)
A	0.0234	86	67	3.6
B	0.0104	87.5	79	2.3
C	0.0233	86	68.5	3.1
D	0.0180	86	75.5	2.9

samples (see Table I). ϕ_0 is the flux quantum and S the array unit cell area. Thus, at $n = 4$ there is one vortex per pinning site. The canonical array [Fig. 1(a)] is characterized by the fact that each hole has three first neighbors at the same distance. This geometry has been used earlier to realize vortex ice [8,32,33] also with interesting temperature effects. In the derived arrays [Figs. 1(b)–1(d)], the distance between the pair of holes marked as L_i , $i = \{1, 2, 3\}$, is gradually reduced relative to the other distances in the array.

We perform simulations of the O^+ irradiation damage to calculate the YBCO local critical temperature underneath and between the mask holes. As we describe in detail elsewhere [34,35], this is done by a combination of Monte Carlo simulations of the irradiation-induced disorder and the application of the Abrikosov-Gorkov depairing law to calculate the T_C depression. An important result of these simulations is that the local critical temperature in between the mask holes strongly depends on the interhole distance. This is because the ion-induced damage increases in the region between mask holes as their separation is shortened. This is illustrated in Fig. 2 with various examples. This figure shows simulations of the local T_C profile along the diameter of two neighboring mask holes, for several interhole distances ranging from 140 to 60 nm. The reduced $t_C = T_C/T_C^{\text{virgin}}$ is displayed, with T_C^{virgin} the critical temperature prior to irradiation. The t_C between holes is lower the shorter the interhole distance is. As discussed below, this has a strong influence on the commensurability between the vortex lattice and the pinning array. This is because the interhole distance is not constant in the studied arrays.

III. RESULTS

Subsequent to ion irradiation, transport measurements are performed in a liquid He flow cryostat equipped with a 0.5-T electromagnet and a rotatable sample holder (0.5° precision). The sample is aligned so that the magnetic field is parallel to the YBCO c axis (i.e., perpendicular to the sample's surface).

Figure 3 shows the normalized resistance R/R_N as a function of temperature in a zero magnetic field, with R_N the normal-state resistance at the onset of the

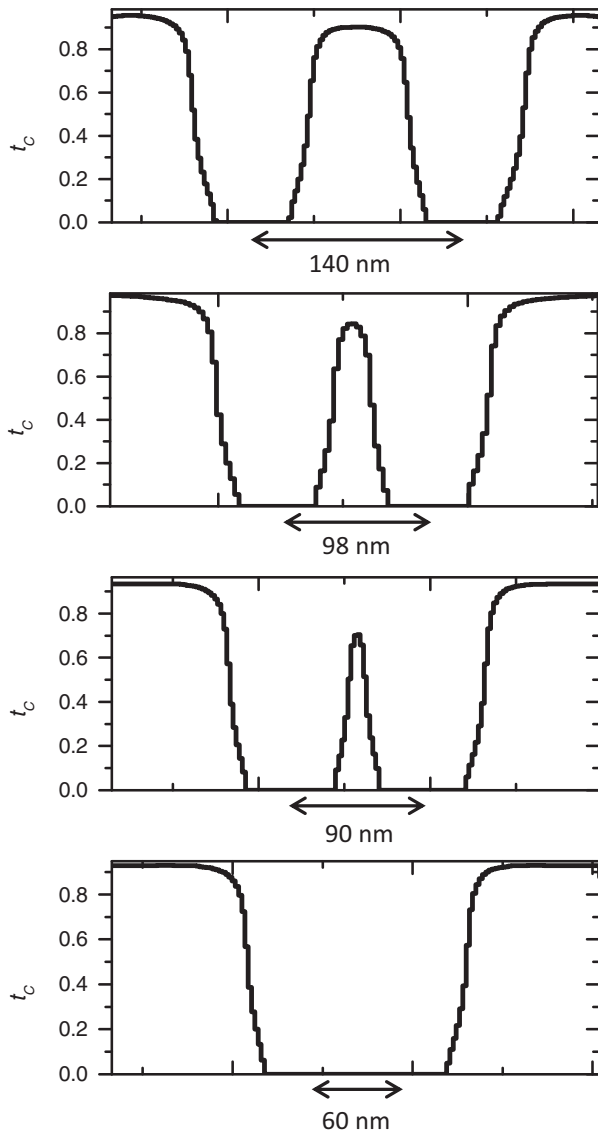


FIG. 2. Simulations of the local superconducting critical temperature t_c modulation for four different interhole distances after the masked O^+ irradiation process. The interhole t_c becomes lower as the holes are placed closer from 140 to 60 nm.

superconducting transition. The curves A–D correspond to the arrays in Figs. 1(a)–1(d), respectively. The resistance $R = V/I$ is obtained from the measured voltage V upon injection of a 5×10^5 A/m² dc current density. The zero-resistance critical temperature T_{C0} is defined as the temperature at which the measured voltage drops below the experimental noise in the setup (approximately 10^{-7} V). The characteristic parameters for the different samples are summarized in Table I.

We investigate flux pinning via magnetotransport measurements at temperatures close to T_{C0} . Figure 4 shows the normalized resistance R/R_N plotted as a function of the applied magnetic field. The latter is expressed as the number of vortices per unit cell n . The curves A–D correspond to the arrays in Figs. 1(a)–1(d), respectively.

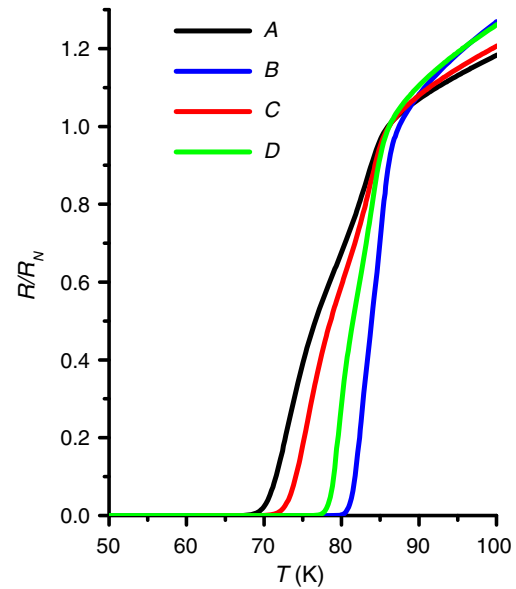


FIG. 3. Normalized resistance R/R_N as a function of temperature in a zero magnetic field for the arrays in Figs. 1(a)–1(d), noted A–D, respectively. R_N is the normal state resistance taken at the onset of the superconducting transition. The injected current density is 5×10^5 Am⁻² in every case.

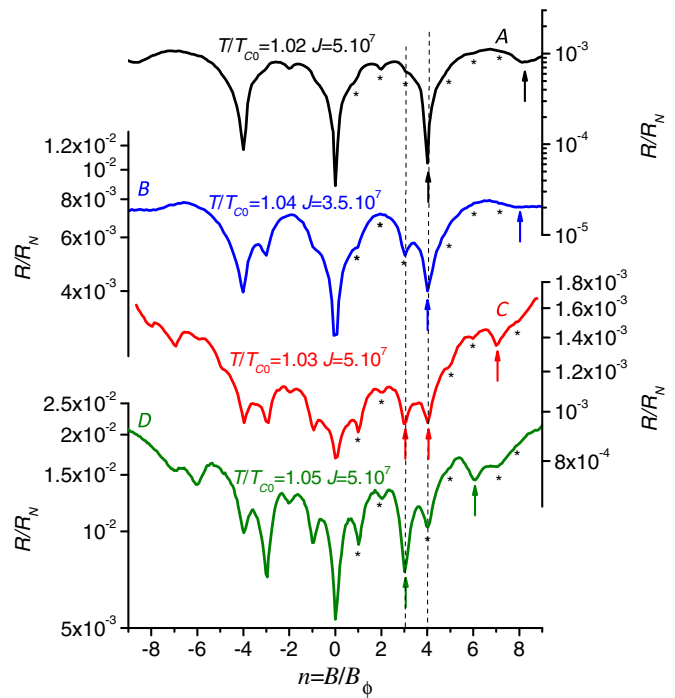


FIG. 4. Normalized resistance R/R_N as a function of the applied magnetic field in units of vortices per unit cell n for the four samples in Figs. 1(a)–1(d), noted A–D, respectively. For each curve, the reduced temperature T/T_{C0} and the injected current density J (in Am⁻²) are given. The two vertical dashed lines highlight the matching effects for $n = 3$ and $n = 4$. Arrows indicate the main minima, while asterisks mark shallower minima.

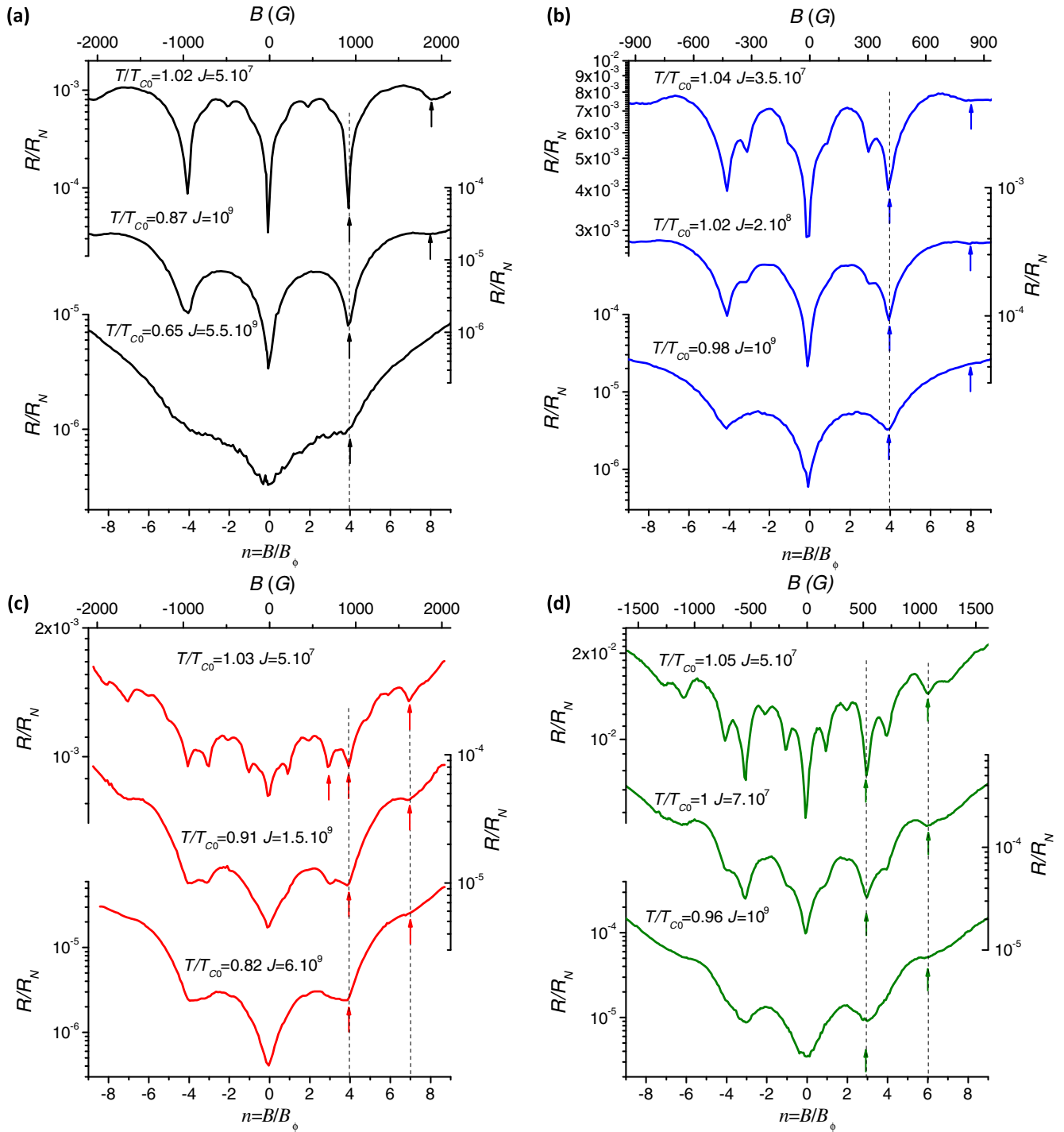


FIG. 5. (a)–(d) Normalized resistance R/R_N as a function of the applied magnetic field in units of vortices per unit cell n for the arrays in Figs. 1(a)–1(d), respectively, at decreasing temperatures. For each curve, the reduced temperature T/T_{c0} and the injected current density J (in Am^{-2}) are given. The vertical dashed lines highlight matching effects for certain vortex densities, and arrows mark the main minima.

All of the curves are completely symmetric. Multiple magnetoresistance dips are observed, which correspond to different commensurability states of the vortex lattice to the pinning array. We observe a striking evolution of the matching effects from array to array. For the canonical

array in Fig. 1(a), the corresponding curve (A in Fig. 4) shows main minima at $|n| = 4$ and $|n| = 8$ (marked with arrows), plus shallower minima (or inflection points) at $|n| = 1, 2, 3$, and barely visible features at $|n| = 5, 6, 7$ (marked with asterisks). For the array D [Fig. 1(d)], the

corresponding curve shows main minima for $|n| = 3$ and $|n| = 6$ (marked with arrows), plus shallower minima (asterisks) at $|n| = 1, 2, |n| = 4, 5$, and then $|n| = 7, 8$. One can therefore describe curve *A* as composed of a large amplitude modulation with a long period ($n = 4$) plus a weaker modulation with a shorter period $n = 1$. Curve *D* shows instead a long-period modulation with $n = 3$ plus a shorter-period ($n = 1$) modulation. The intermediate curves corresponding to arrays *B* [shown Fig. 1(b)] and *C* [shown Fig. 1(c)] can be viewed as a gradual evolution between the two limiting cases (*A* and *D*). This becomes evident, for instance, if we focus on the relative intensity of the $|n| = 3$ and $|n| = 4$ minima (marked with dashed lines). For the canonical array *A*, $|n| = 4$ are the deepest while the minima at $|n| = 3$ are barely visible. In curve *B* (blue curve), $|n| = 4$ are still the deepest of the series, but those at $|n| = 3$ become more pronounced than in *A*. This tendency is exacerbated for sample *C* (red curve), in which the minima at $|n| = 3$ and $|n| = 4$ are of identical intensity. Finally, for sample *D* (green curve), the minima for $|n| = 3$ become the deepest at the expense of those at $|n| = 4$. Additionally, we can see that the high-order main minima go from $|n| = 8$ for samples *A* and *B* to $|n| = 7$ for *C* and $|n| = 6$ for *D*.

Figure 5 shows magnetotransport experiments at different temperatures. Upon a temperature decrease, we observe a general smoothing of the curves. In all cases, the shallowest (short-period) oscillations in between the main minima gradually fade away. At the lowest T , only the main minima (corresponding to the long-period modulation) remain. Interestingly, the way in which this happens is different for the different samples. In Figs. 5(a) and 5(b), the minima at $|n| = 4$ (and their first harmonic $|n| = 8$) remain the most intense at low T . In Fig. 5(d), those at $|n| = 3$ (and their first harmonic $|n| = 6$) prevail at low T . At variance, a striking behavior is observed in Fig. 5(c): The relative intensity of the minima at $|n| = 3$ and $|n| = 4$, initially identical, is unbalanced in favor of $|n| = 4$, which become the most intense at low T . Notwithstanding, the higher-order minima do not correspond to the first harmonic $|n| = 8$, but to $|n| = 7$, at any temperature.

IV. DISCUSSION

Let us now explain the series of minima for the different arrays.

For the canonical array *A* [Fig. 1(a)], the most intense matching effects appear at $|n| = 4$ and its harmonics, for which there is an integer number of vortices per pinning site [see the sketch in Fig. 6(a) for $|n| = 4$]. The shallower minima in between them correspond to “fractional matching” [31,36], in which there is a noninteger number of vortices per array pinning site, resulting in weaker pinning [8].

The behaviors of samples *B–D* can be explained by considering the simulations of the local critical temperature between holes shown in Fig. 2. Contrary to array *A*, in

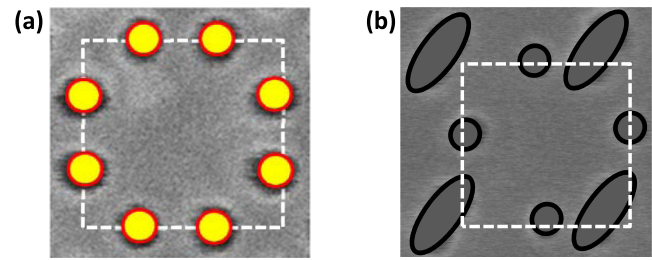


FIG. 6. (a) Schematic representations of the inferred vortex distribution (yellow circles) from magnetoresistance experiments for the array in Fig. 1(a). (b) Effective energy landscape for the array in Fig. 1(c) at high temperatures. The merging of pinning sites is represented by black ovals. The white dashed square indicates the array unit cell in both cases. In (b), the total number of sites in the unit cell is 3: four $1/2$ pinning sites (circular sites), plus two $1/4$ from the top and lower left oval sites, and $1/2$ from the lower right oval site.

arrays *B–D* not all of each pinning site’s neighbors are at the same distance; this is shorter along L_1 , L_2 , and L_3 (respectively, for arrays *B*, *C*, and *D*) than in between the rest of the pinning sites within the unit cell. As expected from Fig. 2, the shorter L_i , the more depressed the local critical temperature in between the pinning sites is, and the lower it is as compared to the local T_C between other pinning sites. The extreme case is that of array *D* [Fig. 1(d)], in which L_3 is so small that the holes are touching and the critical temperature between them is completely suppressed (as in the bottom curve of Fig. 2). This means that the irradiation process has effectively merged those two pinning sites, creating a single oval-shaped one. As a result, the unit cell contains only three pinning sites (one oval shaped and two circular ones) instead of four. Thus, as expected from the well-known behavior of regular arrays [31,36], the main matching fields for this sample appear at $|n| = 3$ and their harmonics, which correspond to an integer number of vortices per pinning site.

Arrays *B* and *C* are at midway between the limiting cases *A* and *D*. In *B* and *C*, the local critical temperature between the closest pinning sites (along L_1 and L_2) is not completely suppressed but somewhat reduced. Thus, the effective height of the energy barrier between them is strongly affected by the temperature, in particular, relative to the barrier between other pinning sites in the unit cell. In this sense, sample *C* is paradigmatic. At a high enough temperature, the similar intensity of the minima for $|n| = 3$ and $|n| = 4$ shows that the vortex configuration is identically stable regardless of whether the closest pinning sites host one or two vortices. This suggests that the energy barrier along L_2 is so small that they behave either as a single composite pinning site or as a pair of them depending on the vortex density. However, when increasing the number of vortices, this ambivalence is broken, and the minima for $|n| = 7 (= 4 + 3)$ prevail over those at $|n| = 8$

(second harmonic of $|n| = 4$). At the lowest temperature, the barrier height along L_2 grows enough to effectively separate the closest sites at low vortex densities, which makes the minima at $|n| = 3$ disappear in favor of those at $|n| = 4$ [see Fig. 5(c)]. However, for higher vortex densities the minima at $|n| = 7$ again prevail even at a low temperature. This suggests that, once the couple of pinning sites separated by L_2 are filled each with a vortex, the energy barrier between both vanishes, so that they subsequently behave as a single (oval-shaped) one, effectively yielding three pinning sites per unit cell [see Fig. 6(b)]. Consequently, we see that, at a high enough temperature or applied magnetic field, there is a modification of the energy landscape due to the tendency of the closest sites to behave as a single (oval-shaped) one.

V. CONCLUSIONS

In summary, we fabricate masked O^+ ion irradiated $YBa_2Cu_3O_{7-\delta}$ thin films with non-Bravais periodic pinning arrays. In a series of samples, the initial fourfold symmetric array is deformed by shortening the distance between some of the pinning sites that form the unit cell. Magnetotransport measurements show that the field at which the strongest matching effect occurs evolves as a function of the deformation of the original array. In particular, the magnetoresistance minima for $n = 4$ vortices per unit cell gradually disappears as the array is deformed in favor of stronger minima for $n = 3$ vortices per unit cell. Upon temperature changes, this tendency can be reversed, and the relative intensity of the minima can be balanced, allowing the tuning of the effective density of pinning sites from four to three sites per unit cell with the temperature and applied field. This is a direct result of the approach with which the pinning landscape is fabricated, a nanoscale spatial modulation of the critical temperature. The ability to tune the geometry and effective number of artificial pinning sites using the temperature as a control knob brings possibilities in the field of vortex manipulation, which may be useful, for instance, to create tunable fluxtronic devices.

ACKNOWLEDGMENTS

This work is supported by the French Agence Nationale de la Recherche (Grant MASTHER, No. 2011-BS03-008-02), COST Action MP1201 “NanoSC,” and the Ville de Paris Emergence Programme. J. T. acknowledges the support of Fundación Barrié (Galicia, Spain).

[1] J. Trastoy, V. Rouco, C. Ulysse, R. Bernard, A. Palau, T. Puig, G. Faini, J. Lesueur, J. Briatico, and J. E. Villegas, Unusual magneto-transport of $YBa_2Cu_3O_{7-\delta}$ films due to the interplay of anisotropy, random disorder and nanoscale periodic pinning, *New J. Phys.* **15**, 103022 (2013).

[2] O. Daldini, P. Martinoli, J. Olsen, and G. Berner, Vortex-Line Pinning by Thickness Modulation of Superconducting Films, *Phys. Rev. Lett.* **32**, 218 (1974).

[3] A. T. Fiory, A. F. Hebard, and S. Somekh, Critical currents associated with the interaction of commensurate flux-line sublattices in a perforated Al film, *Appl. Phys. Lett.* **32**, 73 (1978).

[4] A. Pruyboom, P. H. Kes, E. van der Drift, and S. Radelaar, Flux-Line Shear through Narrow Constraints in Superconducting Films, *Phys. Rev. Lett.* **60**, 1430 (1988).

[5] Y. Otani, B. Pannetier, J. P. Nozières, and D. Givord, Magnetostatic interactions between magnetic arrays and superconducting thin films, *J. Magn. Magn. Mater.* **126**, 622 (1993).

[6] M. Baert, V. V. Metlushko, R. Jonckheere, V. V. Moshchalkov, and Y. Bruynseraede, Composite Flux-Line Lattices Stabilized in Superconducting Films by a Regular Array of Artificial Defects, *Phys. Rev. Lett.* **74**, 3269 (1995).

[7] J. I. Martín, M. Vélez, J. Nogués, and I. K. Schuller, Flux Pinning in a Superconductor by an Array of Submicrometer Magnetic Dots, *Phys. Rev. Lett.* **79**, 1929 (1997).

[8] J. Trastoy, M. Malnou, C. Ulysse, R. Bernard, N. Bergeal, G. Faini, J. Lesueur, J. Briatico, and J. E. Villegas, Freezing and thawing of artificial ice by thermal switching of geometric frustration in magnetic flux lattices, *Nat. Nanotechnol.* **9**, 710 (2014).

[9] B. Y. Zhu, F. Marchesoni, V. V. Moshchalkov, and F. Nori, Controllable step motors and rectifiers of magnetic flux quanta using periodic arrays of asymmetric pinning defects, *Phys. Rev. B* **68**, 014514 (2003).

[10] J. E. Villegas, S. Savel’ev, F. Nori, E. M. Gonzalez, J. V. Anguita, R. García, and J. L. Vicent, A superconducting reversible rectifier that controls the motion of magnetic flux quanta, *Science* **302**, 1188 (2003).

[11] C. Reichhardt and C. J. Olson, Reichhardt, Moving vortex phases, dynamical symmetry breaking, and jamming for vortices in honeycomb pinning arrays, *Phys. Rev. B* **78**, 224511 (2008).

[12] G. Karapetrov, V. Yefremenko, G. Mihajlović, J. E. Pearson, M. Iavarone, V. Novosad, and S. D. Bader, Evidence of vortex jamming in Abrikosov vortex flux flow regime, *Phys. Rev. B* **86**, 054524 (2012).

[13] S. Field, J. Witt, F. Nori, and X. Ling, Superconducting Vortex Avalanches, *Phys. Rev. Lett.* **74**, 1206 (1995).

[14] E. Althuler and T. H. Johansen, Colloquium: Experiments in vortex avalanches, *Rev. Mod. Phys.* **76**, 471 (2004).

[15] P. T. Korda, G. C. Spalding, and D. G. Grier, Evolution of a colloidal critical state in an optical pinning potential landscape, *Phys. Rev. B* **66**, 024504 (2002).

[16] P. de Gennes, Wetting: Statics, and dynamics, *Rev. Mod. Phys.* **57**, 827 (1985).

[17] P. Paruch, T. Giamarchi, T. Tybell, and J.-M. Triscone, Nanoscale studies of domain wall motion in epitaxial ferroelectric thin films, *J. Appl. Phys.* **100**, 051608 (2006).

[18] S. Lemerle, J. Ferré, C. Chappert, V. Mathet, T. Giamarchi, and P. Le Doussal, Domain Wall Creep in an Ising Ultrathin Magnetic Film, *Phys. Rev. Lett.* **80**, 849 (1998).

[19] L. Krusin-Elbaum, T. Shibauchi, B. Argyle, L. Gignac, and D. Weller, Stable ultrahigh-density magneto-optical

- recordings using introduced linear defects, *Nature (London)* **410**, 444 (2001).
- [20] S.-Z. Lin, C. Reichhardt, C. D. Batista, and A. Saxena, Driven Skyrmions and Dynamical Transitions in Chiral Magnets, *Phys. Rev. Lett.* **110**, 207202 (2013).
- [21] A. Fert, V. Cros, and J. Sampaio, Skyrmions on the track, *Nat. Nanotechnol.* **8**, 152 (2013).
- [22] S. Ooi, S. Savel'ev, M. Gaifullin, T. Mochiku, K. Hirata, and F. Nori, Nonlinear Nanodevices Using Magnetic Flux Quanta, *Phys. Rev. Lett.* **99**, 207003 (2007).
- [23] M. B. Hastings, C. J. Olson Reichhardt, and C. Reichhardt, Ratchet Cellular Automata, *Phys. Rev. Lett.* **90**, 247004 (2003).
- [24] M. V. Milošević, G. R. Berdiyrov, and F. M. Peeters, Fluxonic cellular automata, *Appl. Phys. Lett.* **91**, 212501 (2007).
- [25] A. Crassous, R. Bernard, S. Fusil, K. Bouzheouane, D. Le Bourdais, S. Enouz-Vedrenne, J. Briatico, M. Bibes, A. Barthélémy, and J. E. Villegas, Nanoscale Electrostatic Manipulation of Magnetic Flux Quanta in Ferroelectric/Superconductor $\text{BiFeO}_3/\text{YBa}_2\text{Cu}_3\text{O}_{7-\delta}$ Heterostructures, *Phys. Rev. Lett.* **107**, 247002 (2011).
- [26] A. Behrooz, M. J. Burns, H. Deckman, D. Levine, B. Whitehead, and P. M. Chaikin, Flux Quantization on Quasicrystalline Networks, *Phys. Rev. Lett.* **57**, 368 (1986).
- [27] J. E. Villegas, M. I. Montero, C. P. Li, and I. K. Schuller, Correlation Length of Quasiperiodic Vortex Lattices, *Phys. Rev. Lett.* **97**, 027002 (2006).
- [28] C. Reichhardt and C. J. Olson Reichhardt, Commensurability effects at nonmatching fields for vortices in diluted periodic pinning arrays, *Phys. Rev. B* **76**, 094512 (2007).
- [29] M. Kemmler, D. Bothner, K. Ilin, M. Siegel, R. Kleiner, and D. Koelle, Suppression of dissipation in Nb thin films with triangular antidot arrays by random removal of pinning sites, *Phys. Rev. B* **79**, 184509 (2009).
- [30] Y. J. Rosen, A. Sharoni, and I. K. Schuller, Enhanced superconducting vortex pinning with disordered nanomagnetic arrays, *Phys. Rev. B* **82**, 014509 (2010).
- [31] I. Swiecicki, C. Ulysse, T. Wolf, R. Bernard, N. Bergeal, J. Briatico, G. Faini, J. Lesueur, and J. E. Villegas, Strong field-matching effects in superconducting $\text{YBa}_2\text{Cu}_3\text{O}_{7-\delta}$ films with vortex energy landscapes engineered via masked ion irradiation, *Phys. Rev. B* **85**, 224502 (2012).
- [32] A. Libál, C. J. Olson Reichhardt, and C. Reichhardt, Creating Artificial Ice States Using Vortices in Nanostructured Superconductors, *Phys. Rev. Lett.* **102**, 237004 (2009).
- [33] M. L. Latimer, G. R. Berdiyrov, Z. L. Xiao, F. M. Peeters, and W. K. Kwok, Realization of Artificial Ice Systems for Magnetic Vortices in a Superconducting MoGe Thin Film with Patterned Nanostructures, *Phys. Rev. Lett.* **111**, 067001 (2013).
- [34] J. Lesueur, P. Nedellec, H. Bernas, J. P. Burger, and L. Dumoulin, Depairing-like variation of T_c in $\text{YBa}_2\text{Cu}_3\text{O}_{7-\delta}$, *Physica (Amsterdam)* **167C**, 1 (1990).
- [35] N. Bergeal, J. Lesueur, M. Sirena, G. Faini, M. Aprili, J. P. Contour, and B. Leridon, Using ion irradiation to make high- T_c Josephson junctions, *J. Appl. Phys.* **102**, 083903 (2007).
- [36] V. Metlushko, U. Welp, G. W. Crabtree, R. Osgood, S. D. Bader, L. E. DeLong, Z. Zhang, S. R. J. Brueck, B. Ilic, K. Chung, and P. J. Hesketh, Interstitial flux phases in a superconducting niobium film with a square lattice of artificial pinning centers, *Phys. Rev. B* **60**, R12585 (1999).